Solvent Exfoliation of Electronic-Grade, Two-Dimensional Black Phosphorus

Joohoon Kang,[†] Joshua D. Wood,[†] Spencer A. Wells,[†] Jae-Hyeok Lee,[†] Xiaolong Liu,[‡] Kan-Sheng Chen,[†] and Mark C. Hersam*[,†,‡,§,∥]

[†]Department of Materials Science and Engineering, [‡]Graduate Program in Applied Physics, [§]Department of Chemistry, and [∥]Department of Medicine, Northwestern University, Evanston, Illinois 60208, United States

ABSTRACT Solution dispersions of two-dimensional (2D) black phosphorus (BP)—often referred to as phosphorene—are achieved by solvent exfoliation. These pristine, electronic-grade BP dispersions are produced with anhydrous organic solvents in a sealed-tip ultrasonication system, which circumvents BP degradation that would otherwise occur *via* solvated O_2 or H_2O. Among conventional solvents, *N*-methylpyrrolidone (NMP) is found to provide stable, highly concentrated (~0.4 mg/mL) BP dispersions. Atomic force microscopy, scanning electron microscopy, transmission electron microscopy, Raman spectroscopy, and X-ray photoelectron spectroscopy show that the structure and chemistry of solvent-exfoliated BP nanosheets are comparable to mechanically exfoliated BP flakes. Additionally, residual NMP from the liquid-phase processing suppresses the rate of BP oxidation in ambient conditions. Solvent-exfoliated BP nanosheet field-effect transistors exhibit ambipolar behavior with current on/off ratios and mobilities up to ~10^4 and ~50 $cm^2\ V^{-1}\ s^{-1}$, respectively. Overall, this study shows that stable, highly concentrated, electronic-grade 2D BP dispersions can be realized by scalable solvent exfoliation, thereby presenting opportunities for large-area, high-performance BP device applications.

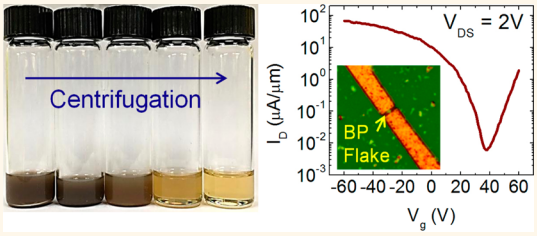

KEYWORDS: phosphorene · liquid phase · anhydrous · organic solvent · centrifugation · degradation · field-effect transistor

Black phosphorus (BP),[1,2] a layered, anisotropic[3,4] allotrope of phosphorus, is emerging as a successor to other two-dimensional (2D) nanomaterials such as graphene[5,6] and transition metal dichalcogenides (TMDs)[7−9] due to its exceptional electronic properties. Unlike semimetallic graphene, BP is a semiconductor with a thickness-dependent, direct band gap ranging from ~0.3 eV in the bulk to ~1.5 eV in the monolayer (*i.e.*, phosphorene) limit.[10−14] Mechanically exfoliated 2D BP possesses current on/off ratios[12,15] of ~10^4−10^5 and room temperature mobilities up to ~200−1000 $cm^2\ V^{-1}\ s^{-1}$.[4,12,15−17] These desirable electronic properties make 2D BP a promising candidate for high-performance electronic and optoelectronic device applications.

Many production methods for 2D nanomaterials have been developed including micromechanical exfoliation,[5,12,18−24] chemical vapor deposition,[25−28] chemical exfoliation,[29,30] and liquid-phase exfoliation.[6,8,31−35] While micromechanical exfoliation generally produces 2D nanomaterials with the highest crystal quality, this method has limited scalability. Conversely, chemical vapor deposition is an effective method for thin-film applications, assuming that suitable precursors can be identified. Large quantities of 2D nanomaterials can also be produced by chemical exfoliation (*e.g.*, lithium intercalation[29] and oxidation[36,37]), but this approach typically introduces defects and/or leads to phase transformations that compromise electronic properties. Alternatively, liquid-phase exfoliation *via* ultrasonication[8] or shear mixing[33] is a viable option to prepare 2D nanomaterials without intermediate chemical reactions.

Recently, it was reported that mechanically exfoliated 2D BP flakes irreversibly degrade to oxidized phosphorus compounds following ambient exposure.[18,23,38] This chemical instability presents challenges for BP liquid-phase exfoliation, in contrast to graphene or TMDs that are sufficiently inert to enable ultrasonic processing in aqueous surfactant solutions. In particular, surfactant micelles in aqueous solution do not fully exclude solvated O_2 or H_2O, allowing potential reactions between BP and these

* Address correspondence to m-hersam@northwestern.edu.

Received for review February 19, 2015 and accepted March 18, 2015.

Published online March 18, 2015
10.1021/acsnano.5b01143

© 2015 American Chemical Society

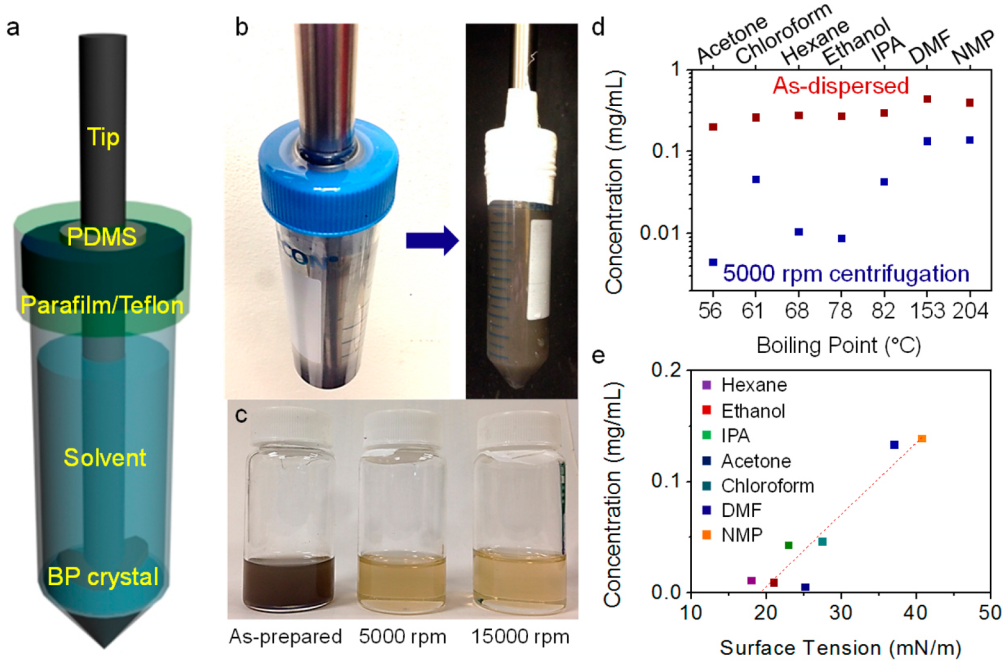

Figure 1. Solvent exfoliation of BP in various solvents *via* tip ultrasonication. (a) Schematic and (b) photograph of the custom-tip ultrasonication setup that minimized exposure to ambient air during processing. (c) Photograph of a BP dispersion in *N*-methylpyrrolidone after ultrasonication, 5000 rpm centrifugation, and 15 000 rpm centrifugation (left to right). (d) BP concentration plot for various solvents with different boiling points before and after 5000 rpm centrifugation and (e) with different surface tensions after 5000 rpm centrifugation.

oxidizing agents.[18] Furthermore, common dispersants for graphene in organic solvents can also degrade BP. For example, BP nanosheets are amorphized by ethyl cellulose (see Supporting Information, Figure S1), which is a conventional dispersant for highly concentrated graphene dispersions.[39,40]

Herein, we present a scalable method for preparing pristine 2D BP nanosheets *via* direct liquid exfoliation in organic solvents. By employing a sealed-tip ultrasonication system, BP is exfoliated into anhydrous, oxygen-free solvents, avoiding the known chemical degradation pathways for 2D BP. The structure, chemistry, and stability of these solvent-exfoliated BP nanosheets are quantified through a comprehensive suite of measurements including atomic force microscopy (AFM), high-resolution transmission electron microscopy (HRTEM), Raman spectroscopy, and X-ray photoelectron spectroscopy (XPS). Finally, field-effect transistors (FETs) are fabricated from individual solvent-exfoliated BP nanosheets to investigate charge transport. By all of these metrics, our solvent-exfoliated 2D BP nanosheets show behavior that is comparable to mechanically exfoliated 2D BP, suggesting their use in a wide range of semiconductor applications.

RESULTS AND DISCUSSION

Bulk BP crystals are exfoliated in organic solvents using ultrasonication procedures that are detailed in the Methods section. Briefly, all BP solution preparation takes place in a dark Ar glovebox using a modified sealed-tip ultrasonicator setup, as shown in Figure 1a,b. The sealed container lid is connected to a 0.125 in. ultrasonicator tip, which is driven at a higher power than typical bath sonication powers in order to minimize the ultrasonication duration (Figure 1a,b). Specifically, ultrasonication in an ice bath at ~30 W power achieves a BP concentration of ~1 mg/mL in 1 h, in contrast to the 15−24 h needed to exfoliate BP *via* bath sonication.[34,35] This reduction in BP sonication time, combined with our anhydrous and anoxic protocol, ultimately preserves the chemical integrity of the BP as will be delineated below. The resulting stable BP dispersions possess a brown to yellow color, as seen in Figure 1c.

Previous graphene studies have found that the choice of organic solvent is critical for efficient solvent exfoliation, with *N*-methylpyrrolidone (NMP) and dimethylformamide (DMF) working particularly well due to their relatively high boiling points and surface tension (~40 mJ/m^2).[32,41] To determine the optimal solvent for BP exfoliation, BP crystals were ultrasonicated in acetone, chloroform, hexane, ethanol, isopropyl alcohol (IPA), DMF, and NMP. Under identical preparation conditions, these anhydrous solvents were opened only in an Ar glovebox to minimize O_2 and H_2O contamination. The as-prepared dispersions were then centrifuged at 500−15 000 rpm for 10 min in an effort to isolate well-exfoliated 2D BP nanosheets, ultimately resulting in the solution color evolving from brown to yellow (Figure 1c). The optical absorbance per cell length (A/l) of the BP dispersions before and after centrifugation is measured at 660 nm. The concentration

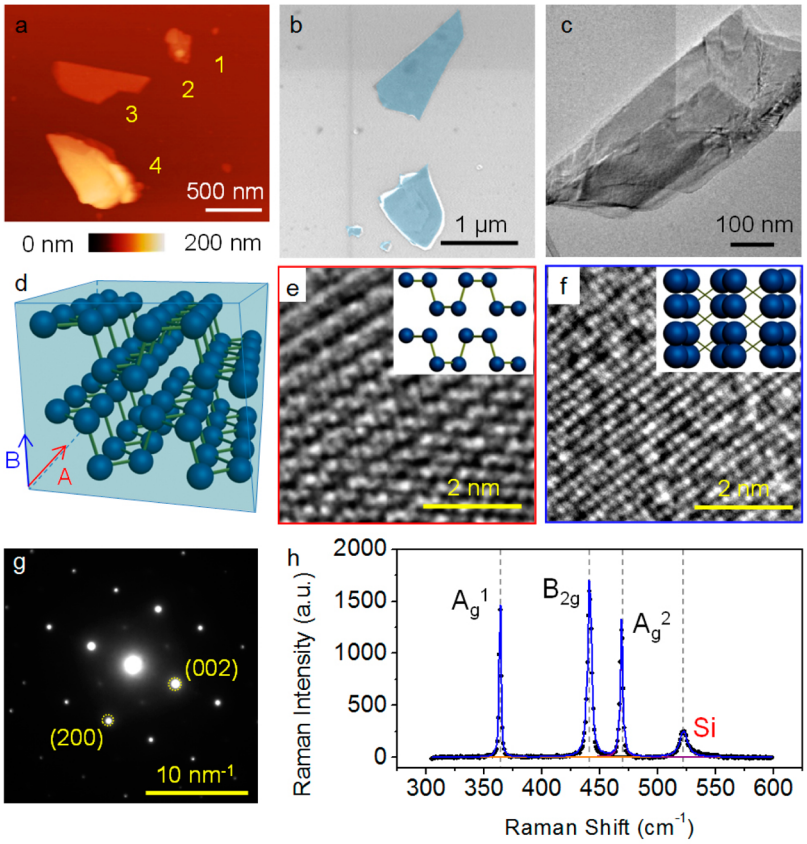

Figure 2. Characterization of solvent-exfoliated BP nanosheets. (a) AFM height image of solvent-exfoliated BP nanosheets that were deposited onto a 300 nm SiO_2/Si substrate with different heights (1:16, 2:40, 3:29, and 4:128 nm). No bubbles or other evidence of degradation are apparent from the solvent exfoliation process. The height data were taken in a N_2 environment. (b) False-colored SEM image of solvent-exfoliated BP nanosheets. (c) Low-resolution TEM image of solvent-exfoliated BP nanosheets. (d) Schematic showing the atomic structure of BP. High-resolution TEM images of solvent-exfoliated BP nanosheets along direction (e) A and (f) B. (g) Selected area electron diffraction pattern of solvent-exfoliated BP nanosheets. (h) Raman spectrum of solvent-exfoliated BP nanosheets.

(C_{BP}) is then determined based on an extinction coefficient (α) of 267 ± 23 Lg^{-1} m^{-1} (Supporting Information, Figure S2). Figure 1d,e shows the BP concentration values for the seven aforementioned solvents, based on their boiling points and surface tension (*A*/*l* at 660 nm are indicated in Table S1). The BP concentration monotonically increases with increasing boiling point and surface tension, which qualitatively matches the trend observed for graphene.[41] Based on these results, NMP was identified as the optimal solvent to achieve stable BP dispersions.

Following exfoliation in NMP, the BP nanosheets were characterized with a comprehensive suite of microscopy and spectroscopy methods. For AFM and SEM analysis, samples were prepared in an Ar glovebox by drop-casting the BP dispersion onto 300 nm SiO_2/Si substrates. In particular, a drop of the BP dispersion was placed on the substrate for ~5 min, after which the sample was blown off with N_2 gas and annealed on a ~70 °C hot plate for ~2 min. In Figure 2a, the deposited BP is imaged with AFM, employing an environmental cell with dry, ultrahigh purity N_2 gas. The AFM height image shows that the thickness values range from 16 to 128 nm. No bubbles, droplets, or other signs of BP degradation are present (Figure 2a).[18] Further AFM studies based on centrifugation speed and ambient degradation will be discussed later. The SEM image of Figure 2b indicates that the lateral dimensions of the BP flakes agree well with the AFM images.

For additional atomic-scale characterization, solvent-exfoliated BP flakes were deposited onto holey carbon TEM grids for HRTEM analysis. Figure 2c shows a low-resolution TEM image of a representative BP nanosheet. A schematic of the BP crystal structure is provided in Figure 2d, revealing the A and B high-symmetry directions. The HRTEM images of Figure 2e,f provide perspectives of these A and B directions, respectively, which are consistent with the inset BP crystal structures. Furthermore, the BP orthorhombic crystalline character is confirmed by a selected area electron diffraction (SAED) pattern, as seen in Figure 2g. Overall, this HRTEM analysis provides strong evidence that BP nanosheets exfoliated by tip sonication maintain their crystalline nature. This conclusion is corroborated by Raman spectroscopy, as given in Figure 2h. Specifically, four modes are observed at ~362, ~439,

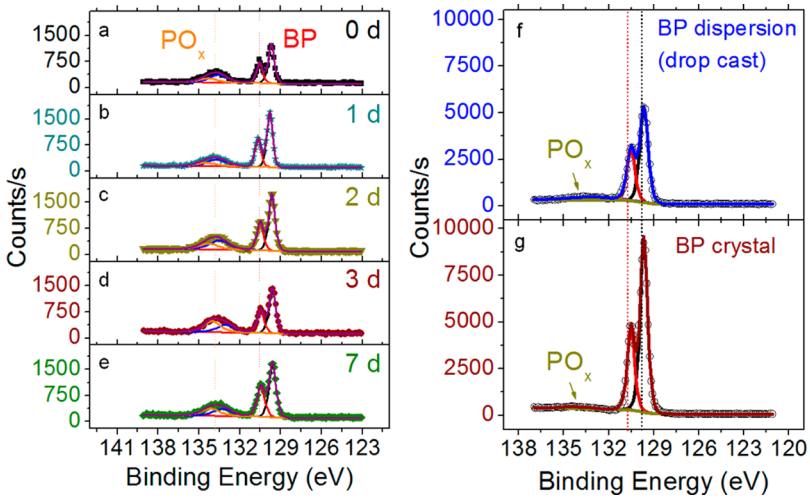

Figure 3. Spectroscopic analysis of ambient-aged BP dispersions *versus* bulk BP crystals. P 2p core-level XPS for drop-casted BP dispersions after (a) 0 days, (b) 1 day, (c) 2 days, (d) 3 days, and (e) 7 days in ambient conditions. The BP flakes are partially oxidized, as confirmed by the PO_x peaks. Oxide content does not increase with exposure time. P 2p core-level spectra for (f) drop-casted BP flakes from dispersion and (g) bulk BP crystals. Both spectra are taken after 10 s of *in situ* sputtering, which removes most of the oxidized BP present.

~467, and ~521 cm^{-1}, which correspond to the A_g^1, B_{2g}, and A_g^2 phonon modes for BP and the TO phonon mode for the silicon substrate (Figure 2h), respectively.[4] The sharp Lorentzian line shapes for the A_g^1, B_{2g}, and A_g^2 modes (1.9, 3.7, and 2.6 cm^{-1}, respectively) are consistent with crystalline BP nanosheets.

The chemical quality of the solvent-exfoliated BP flakes is assessed using XPS in Figure 3. The BP samples for XPS analysis are prepared using the same procedure as described for Figure 2. For reference, a BP bulk crystal (from HQ Graphene) is also measured. The solvent-exfoliated BP nanosheets are monitored as a function of ambient exposure time in order to facilitate comparison with mechanically exfoliated BP, whose ambient oxidization kinetics are known.[18] Figure 3a shows that the as-prepared BP flakes have the $2p^{3/2}$ and $2p^{1/2}$ doublet at 129.7 and 130.5 eV, respectively, characteristic of crystalline BP.[18,42−44] Small oxidized phosphorus (*i.e.*, PO_x) sub-bands are also apparent at ~134 eV, as observed in previous measurements.[18,42−44] These PO_x sub-bands likely stem from oxygen defects[45] or surface suboxides in the BP, which are introduced during solvent exfoliation. Nevertheless, these defects do not significantly compromise the electronic characteristics of the BP nanosheets, as will be detailed later. Figure 3b−e reveals that, despite 1, 2, 3, and 7 days of ambient exposure, the BP nanosheets have a similar oxide content, demonstrating slowed ambient degradation kinetics for solvent-exfoliated BP nanosheets compared to mechanically exfoliated BP.[18]

In Figure 3f,g, *in situ* sputtering is employed to remove the obscuring oxygen defects in both solvent-exfoliated BP nanosheets and bulk BP crystals. In this manner, the solvent-exfoliated BP nanosheets can be compared against a chemically, electronically, and structurally pure standard. The XPS spectra are taken after sputtering the solvent-exfoliated BP sample for 10 s (~2.4 nm BP material removed) and the bulk BP crystal for 60 s (~14.4 nm removed). Figure 3f,g shows P 2p core-level XPS data for these two cases. Both spectra have weak PO_x sub-bands after sputtering, resulting from trace amounts of oxygen defects in the samples. When compared against the BP bulk crystal, the solvent-exfoliated BP sample has a lower XPS signal intensity, due to a lower amount of BP material present. Other than the signal intensity, however, the two spectra are indistinguishable, further reinforcing the high chemical quality of the solvent-exfoliated BP nanosheets.

In order to tailor the size distribution of solvent-exfoliated BP nanosheets, the dispersed BP solutions are centrifuged at different speeds. In Figure 4a, the solution color proceeds from dark brown to light yellow as higher centrifugation speeds are applied. Figure 4b reveals the correlation between centrifugation speed and overall BP concentration, with the light yellow solution ("5") possessing the most dilute concentration (~0.01 mg/mL) of BP nanosheets. In addition, the flake thickness and lateral size decrease with increasing centrifugation, as determined by AFM and shown in Figure 4c. The BP dispersions centrifuged at 500 rpm possess a significant number of thick BP nanosheets (>50 nm thick BP outliers are indicated in Figure S3). In contrast, BP dispersions following 10 000 and 15 000 rpm centrifugation minimize the BP nanosheet lateral size. Finally, BP dispersions centrifuged at 5000 rpm result in thin BP flakes with relatively large lateral area, which will be used for the charge transport measurements described below.

To determine suitable processing conditions for solvent-exfoliated BP devices, an ambient degradation

study was performed using AFM. Recently, Wood *et al.* reported that topographic protrusions (hereafter called bubbles) were found within mechanically exfoliated BP nanosheets shortly after exfoliation.[18] Structural modifications such as bubble formation in BP flakes are an indication of irreversible BP oxidation into phosphate derivatives, ultimately destroying the high-performance electronic properties of BP. Five different samples were prepared on identical 300 nm SiO_2/Si substrates to assess potential solvent-exfoliated BP structural modification in ambient conditions. Figure 5 shows AFM amplitude images for BP samples prepared by mechanical exfoliation, liquid exfoliation in NMP, and mechanical exfoliation with 1 h dipping in NMP. In addition, Figure S6 gives further AFM data for atomic layer deposition (ALD) alumina-encapsulated samples produced by solvent exfoliation in NMP and mechanical exfoliation. After sample preparation, all samples were stored in dark, ambient conditions with an average temperature of 26.9 ± 0.2 °C and a relative humidity of 21.2 ± 0.4%.

In Figure 5, no bubbles or other evidence of degradation are observed for all BP samples shortly after sample preparation (red arrows). After 1 day in ambient conditions, bubbles (blue arrows) are apparent only on the mechanically exfoliated BP surface, corroborating recently reported results.[18] After 2 days, bubbles are also found on the solvent-exfoliated BP sample and the mechanically exfoliated BP sample with 1 h NMP exposure. These degradation bubbles occur after 2 days, regardless of flake thickness or lateral size (see Figures S4 and S5). After 7 days, we note that

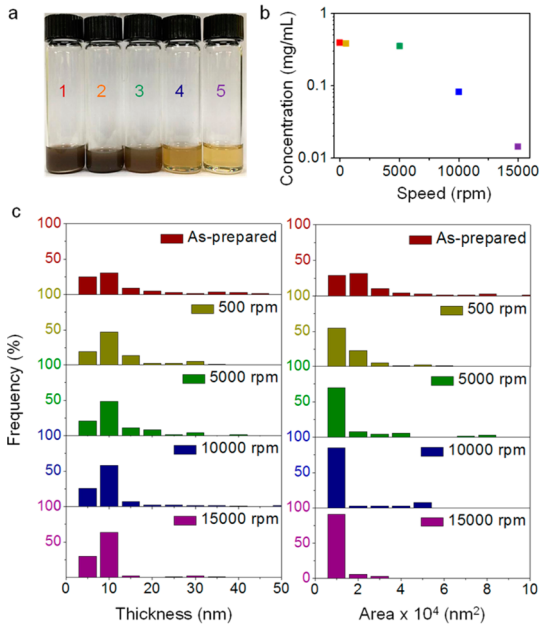

Figure 4. Concentration, thickness, and lateral area distribution of solvent-exfoliated BP with different centrifugation speeds. (a) Photograph of BP dispersions in NMP following different centrifugation conditions (1, as-prepared, 2:500 rpm, 3:5000 rpm, 4:10000 rpm, and 5:15000 rpm). (b) Concentration of the five BP dispersions from part (a). (c) Thickness and lateral area histograms of the five BP dispersions from part (a) as obtained from AFM images.

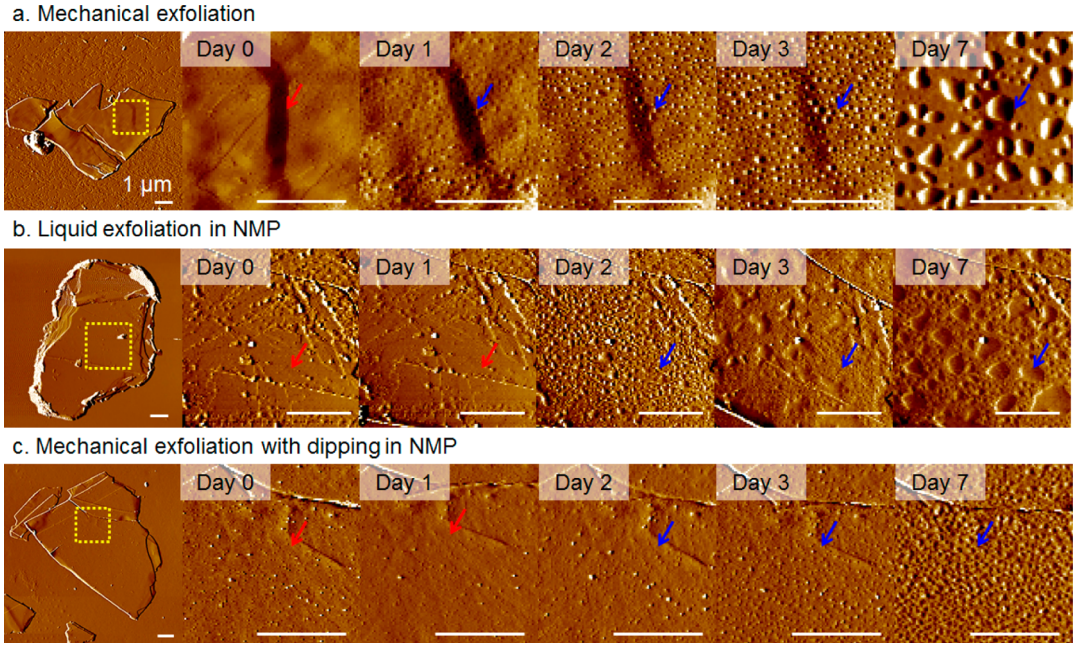

Figure 5. AFM amplitude images (amplitude scale: −5 to 5 nm (top left), −1 to 1 nm (magnified images)) of BP flakes prepared by (a) mechanical exfoliation, (b) solvent exfoliation in NMP, and (c) mechanical exfoliation followed by 1 h submersion in NMP. The leftmost image shows the entire flake, and the images progressing to the right show magnified views immediately after exfoliation up to 7 days in ambient conditions. Structural deformations (*i.e.*, apparent bubbles) are observable on the mechanically exfoliated sample after 1 day and on the rest of the samples after 2 days. Red and blue arrows indicate the same position on the BP flake before and after the appearance of bubbles, respectively. All flakes are thicker than 150 nm, and all scale bars are 1 μm.

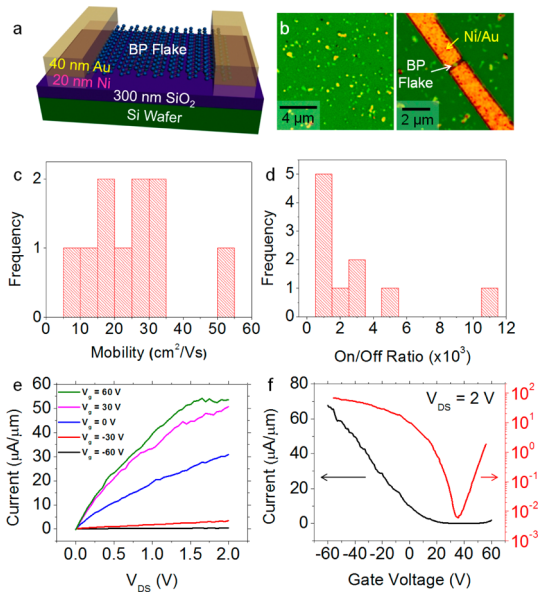

Figure 6. Charge transport measurements of solvent-exfoliated BP FETs. (a) BP FET device schematic. (b) Optical microscopy images after thin-film transfer using PDMS stamping (left) and after device fabrication (right). Histograms of (c) mobility and (d) on/off ratio for a series of solvent-exfoliated BP FETs. (e) Output curves for a solvent-exfoliated BP FET. (f) Transfer curve for a solvent-exfoliated BP FET. The drain current is indicated as a function of gate voltage on a linear scale (black, left) and a logarithmic scale (red, right).

the bubbles coarsen, forming larger and taller bubbles on all three samples. Here, the red and blue arrows indicate the same position before and after the appearance of bubbles. From these results, it appears that residual NMP retards BP degradation for about 24 h of total ambient exposure, potentially originating from NMP encapsulation or intercalation. Control AFM measurements on solvent-exfoliated and mechanically exfoliated BP samples passivated with ALD alumina overlayers do not show any degradation bubbles after 7 days, as expected (Figure S6). Overall, these results underscore that solvent-exfoliated BP nanosheets possess comparable, if not slightly improved, ambient stability, thus enabling reliable device fabrication and charge transport measurements.

To explore the electrical properties of solvent-exfoliated BP nanosheets, FET devices were fabricated on individual BP flakes by electron beam lithography (EBL) using metal electrodes consisting of 20 nm Ni and 40 nm Au, as shown in Figure 6a. To enable high device yield, dispersions were prepared with BP nanosheet lateral dimensions suitable for EBL processing and thicknesses (t) that are expected to demonstrate semiconducting behavior (t < 10 nm). Based upon the lateral size and thickness histograms (Figure 4b,c), BP dispersions were centrifuged at 5000 rpm to achieve a distribution of BP nanosheets with proper thickness and lateral size. To further increase the number density of the BP nanosheets, the BP nanosheets were collected on anodic aluminum oxide (AAO) membranes with 20 nm pore size *via* vacuum filtration. The BP flakes on these membranes were then transferred onto 300 nm SiO_2/Si substrates using polydimethylsiloxane (PDMS) stamping. From optical microscopy imaging in Figure 5b, the highly packed BP nanosheets were found to have a color contrast of dark green to light yellow (Figure 5b, left). This level of BP nanosheet surface coverage facilitated the fabrication of individual BP nanosheet FETs. However, we note that our protocol may be modified to achieve degradation-free, continuous BP thin films by controlling substrate wettability with surface pretreatments,[18] by intercalating lithium to increase exfoliation yield,[29] or by employing Langmuir–Blodgett thin-film deposition techniques.[46] Although the BP nanosheets were exposed to ambient conditions for ~60 to 90 min during this processing, the results of Figure 5 suggest that degradation on this time scale is minimal. The right side of Figure 6b shows the as-fabricated, solvent-exfoliated BP FET.

FET measurements reveal ambipolar behavior for solvent-exfoliated BP with a median hole mobility of 25.9 $cm^2\ V^{-1}\ s^{-1}$ and I_{on}/I_{off} ratio of 1.6×10^3. To demonstrate the reproducibility of these transport results, mobility and I_{on}/I_{off} ratio histograms from as-fabricated, solvent-exfoliated BP FETs are presented in Figure 6c,d. The solution-processed BP FETs uniformly show current saturation and ambipolar transfer characteristics. In Figure 6e,f, the transfer and output curves are shown for our champion, solution-processed BP FET, having an I_{on}/I_{off} ratio of ~10^4. The transfer curve of a BP FET showing both gate voltage sweep directions is shown in Figure S7a. The observed level of hysteresis is comparable to previous results on micromechanically exfoliated BP FETs.[18,23] It should also be noted that the field-effect mobility extracted from the forward sweep (75.5 $cm^2/V \cdot s$) is consistently higher than the mobility extracted from the reverse sweep (Figure S7b). Overall, these FET results are comparable to micromechanically exfoliated BP, further indicating that our solvent exfoliation method does not compromise electrical or structural properties.

CONCLUSION

In summary, a solvent-based exfoliation method is presented that produces electronic-grade BP nanosheets using a sealed-tip ultrasonicator at high power output in an inert environment. The solvent-exfoliated BP nanosheets are then characterized with a comprehensive set of microscopic and spectroscopic analysis techniques, revealing structural and chemical properties that are comparable to mechanically exfoliated BP. Furthermore, AFM measurements as a function of ambient exposure show that residual NMP provides a reduction in the ambient degradation kinetics for solvent-exfoliated BP compared to mechanically

exfoliated BP. This stability coupled with the appropriate centrifugal size selection of solvent-exfoliated BP nanosheets allows for the reliable preparation of FET devices. The resulting charge transport measurements show that the solvent-exfoliated BP nanosheets possess ambipolar behavior with device metrics that are competitive with mechanically exfoliated BP. All of our microscopic, spectroscopic, and electronic transport measurements demonstrate that our liquid-phase exfoliated BP nanosheets rival the characteristics of pristine, mechanically exfoliated BP flakes. The ability to produce electronic-grade BP nanosheets *via* scalable solution processing will accelerate ongoing efforts to realize large-area 2D BP electronic and optoelectronic applications.

METHODS

Solvent Exfoliation. Black phosphorus crystals were purchased from a commercial supplier (Smart-Elements) and stored in a dark Ar glovebox. All BP crystal storage containers were annealed in the Ar glovebox (>100 °C) to remove adventitious H_2O. For solvent exfoliation experiments, a custom-tip sonicator setup was prepared by perforating the plastic lid of a 50 mL conical tube with a 0.125 in. sonicator tip. The interface between the tip and the lid was sealed with PDMS several times, preventing O_2 and H_2O penetration into the tube (see Figure 1a,b). Additionally, Parafilm and Teflon tapes were used to further suppress potential O_2 or H_2O pathways between the lid and container. Therefore, only BP crystals, anhydrous solvent, and Ar gas were present in the conical tube during sonication. The BP crystal and organic solvent were placed in this sealed conical tube with the sonicator tip in an Ar glovebox. The container was then connected to the sonicator (Fisher Scientific model 500 sonic dismembrator) in ambient conditions, after which the BP crystal was exfoliated *via* ultrasonication. As-prepared BP dispersions were centrifuged with different speeds to remove unexfoliated BP crystals using an Eppendorf tabletop centrifuge (Figure 1c).

Extinction Coefficient Measurements. Different volumes of BP dispersion in NMP after centrifugation were vacuum filtered on AAO membranes possessing a ~20 nm pore size. The concentration of dispersed BP was calculated by measuring the weight difference of the AAO membrane before and after vacuum filtration. Furthermore, the optical absorbance per cell length (A/l) was determined from optical absorbance spectra at 660 nm (Cary 5000 spectrophotometer, Agilent Technologies). Using Beer's law ($A/l = \alpha C_{BP}$), the BP extinction coefficient was extracted from the slope of a plot of A/l *versus* concentration (Figure S2).

Atomic Force Microscopy. All height and amplitude measurements were performed in tapping mode using an Asylum Cypher AFM with Si cantilevers (~290 kHz resonant frequency). Images were taken in the repulsive phase regime using a minimum of 512 samples per line. The scanning rate was ~0.4 Hz. AFM imaging employing N_2 flow was performed in an environmental cell attached to the Cypher ES scanner. After the BP was deposited onto the substrate, the environmental cell was assembled in the Ar glovebox and attached to an ultrahigh purity grade N_2 flowing tube. BP flakes of interest for AFM scanning were identified *in situ* with the built-in optical microscope in the Cypher system. During AFM scanning, N_2 was continuously flowed through the cell with the optical microscope light illuminated.

For the AFM ambient degradation study, all samples were prepared in the Ar glovebox and transferred onto the normal sample holder exposed to ambient conditions, with fewer than 30 min of exposure to ambient air before selecting BP flakes of interest with the built-in optical microscope and initiating the AFM image scan.

Scanning Electron Microscopy. SEM images using a secondary electron detector were acquired on a Hitachi SU 8030 FE-SEM. The acceleration voltage was 2 keV, and the beam current was ~10 μA. Images were acquired in fewer than 40 s to mitigate sample charging and electron-beam-induced deposition of carbon.

Transmission Electron Microscopy. A droplet of BP dispersion was deposited on a holey carbon TEM grid (Ted-Pella) and fully dried in an Ar glovebox. The TEM grid was then loaded in the TEM sample holder with fewer than 5 min of exposure to ambient air. The TEM measurement was performed with a JEOL JEM-2100 TEM at an accelerating voltage of 200 keV.

Raman Spectroscopy. Raman spectra were obtained using an Acton TriVista confocal Raman system with an excitation wavelength of 514 nm. Data were collected for 30 s at ~0.1 mW using a 100× objective.

X-ray Photoelectron Spectroscopy. An ultrahigh vacuum (UHV) Thermo Scientific ESCALAB 250 Xi XPS system was used at a base pressure of $\sim 5 \times 10^{-10}$ Torr to gather XPS data. The XPS data had a binding energy resolution of ~0.1 eV using a monochromated Al Kα X-ray source at ~1486.7 eV (~400 μm spot size). Solvent-exfoliated BP thin films on SiO_2/Si were charge compensated using a flood gun. No flood gun compensation was used for bulk BP crystals (HQ Graphene, The Netherlands). Bulk BP crystals were in electrical contact with the stage by UHV-compatible, double-sided Cu tape. All core-level spectra were the average of five scans taken at a 100 ms dwell time using a pass energy of 15 eV. When using charge compensation, all core levels were charge corrected to adventitious carbon at ~284.8 eV. A 3000 keV ion gun (~0.24 nm/s etch rate) was used to perform depth profiling. Using the software suite Avantage (Thermo Scientific), all subpeaks were determined in a manner detailed elsewhere.[18] The p core levels for phosphorus and silicon were fitted with doublets.

Electron Beam Lithography. Features were defined with EBL in poly(methyl methacrylate). To make electrical contact to the flake, 20 nm of Ni and 40 nm of Au were used as the contact metals. To minimize BP degradation, fewer than 24 h elapsed between exfoliation and charge transport measurements.

Atomic Layer Deposition. ALD of alumina was performed with H_2O and trimethylaluminum (TMA) precursors in a Cambridge NanoTech reactor. For the AFM stability studies detailed in the Supporting Information, ~3 nm of alumina was deposited at room temperature. During the ALD process, pulses of TMA precursor were introduced before those of H_2O in an effort to scavenge any adventitious oxygen or H_2O. To form a seed layer and protect BP from potential damage due to high-temperature exposure to oxygenated H_2O, the first ~3 nm was deposited at room temperature with prolonged purge time for both H_2O and TMA. Subsequently, the remainder of the film was deposited at 150 °C with a normal purge time. No other seeding layers were used in the processing.

Charge Transport Measurements. Electrical measurements of BP FETs were performed in a Lakeshore CRX 4K probe station at less than 5×10^{-4} Torr pressure at room temperature. Two Keithley sourcemeter 2400 units were used to measure the current–voltage characteristics. Equation 1 was used to calculate mobility in Figure 6:

$$\mu_{\text{eff}} = \frac{L g_{\text{d}}}{W C_{\text{ox}} V_{\text{DS}}} \quad (1)$$

where μ_{eff} is the field-effect mobility, L is the channel length (obtained from optical micrographs), g_{d} is the transconductance, W is the channel width (obtained from optical micrographs), C_{ox} is the oxide capacitance (11 nF·cm^{-2} for 300 nm thick thermal SiO_2), and V_{DS} is the applied source–drain bias.

Conflict of Interest: The authors declare no competing financial interest.

Acknowledgment. Solution processing and Raman spectroscopy were supported by the National Science Foundation (DMR-1006391); AFM and XPS were supported by the Office of Naval Research (N00014-14-1-0669); electron microscopy was supported by the Department of Energy (DE-FG02-09ER16109); and charge transport measurements were supported by the National Science Foundation Materials Research Science and Engineering Center (DMR-1121262). This work made use of the NUANCE Center, which has received support from the NSF MRSEC (DMR-1121262), the State of Illinois, and Northwestern University. S.A.W. was supported under contact FA9550-11-C-0028 from the Department of Defense, Air Force Office of Scientific Research, National Defense Science and Engineering Graduate (NDSEG) Fellowship, 32 CFR 168a. The authors kindly thank Dr. Jinsong Wu and Dr. Shuyou Li for their help with TEM measurements. The authors also acknowledge fruitful discussions with Christopher Ryder. J.K., J.D.W., S.A.W., and M.C.H. planned the experiments. J.K. performed solution processing, AFM, Raman spectroscopy, and thin-film transfer. J.D.W. prepared mechanically exfoliated BP from bulk crystals and performed XPS. S.A.W. prepared devices by electron beam lithography and measured charge transport. J.-H.L. and J.K. performed the AFM ambient stability study. X.L. collected HRTEM and SAED data. K.-S.C. and J.K. collected AFM data in the environmental cell. The manuscript was written through contributions of all authors. M.C.H. supervised the project.

Supporting Information Available: Additional data and analysis including HRTEM images, extinction coefficient measurements, solvent-exfoliated BP thickness histograms, AFM height images of solvent-exfoliated BP flakes, AFM amplitude images of BP flakes encapsulated by ALD, and BP FET hysteresis results. This material is available free of charge *via* the Internet at http://pubs.acs.org.

REFERENCES AND NOTES

1. Brown, A.; Rundqvis, S. Refinement of Crystal Structure of Black Phosphorous. *Acta Crystallogr.* **1965**, *19*, 684–685.
2. Jamieson, J. C. Crystal Structures Adopted by Black Phosphorus at High Pressures. *Science* **1963**, *139*, 1291–1292.
3. Fei, R. X.; Yang, L. Strain-Engineering the Anisotropic Electrical Conductance of Few-Layer Black Phosphorus. *Nano Lett.* **2014**, *14*, 2884–2889.
4. Xia, F. N.; Wang, H.; Jia, Y. C. Rediscovering Black Phosphorus as an Anisotropic Layered Material for Optoelectronics and Electronics. *Nat. Commun.* **2014**, *5*, 4458.
5. Novoselov, K. S.; Jiang, D.; Schedin, F.; Booth, T. J.; Khotkevich, V. V.; Morozov, S. V.; Geim, A. K. Two-Dimensional Atomic Crystals. *Proc. Natl. Acad. Sci. U.S.A.* **2005**, *102*, 10451–10453.
6. Green, A. A.; Hersam, M. C. Solution Phase Production of Graphene with Controlled Thickness *via* Density Differentiation. *Nano Lett.* **2009**, *9*, 4031–4036.
7. Jariwala, D.; Sangwan, V. K.; Lauhon, L. J.; Marks, T. J.; Hersam, M. C. Emerging Device Applications for Semiconducting Two-Dimensional Transition Metal Dichalcogenides. *ACS Nano* **2014**, *8*, 1102–1120.
8. Kang, J.; Seo, J. W.; Alducin, D.; Ponce, A.; Yacaman, M. J.; Hersam, M. C. Thickness Sorting of Two-Dimensional Transition Metal Dichalcogenides *via* Copolymer-Assisted Density Gradient Ultracentrifugation. *Nat. Commun.* **2014**, *5*, 5478.
9. Kim, I. S.; Sangwan, V. K.; Jariwala, D.; Wood, J. D.; Park, S.; Chen, K. S.; Shi, F. Y.; Ruiz-Zepeda, F.; Ponce, A.; Jose-Yacaman, M.; et al. Influence of Stoichiometry on the Optical and Electrical Properties of Chemical Vapor Deposition Derived MoS_2. *ACS Nano* **2014**, *8*, 10551–10558.
10. Takao, Y.; Asahina, H.; Morita, A. Electronic-Structure of Black Phosphorus in Tight-Binding Approach. *J. Phys. Soc. Jpn.* **1981**, *50*, 3362–3369.
11. Akahama, Y.; Endo, S.; Narita, S. Electrical-Properties of Black Phosphorus Single-Crystals. *J. Phys. Soc. Jpn.* **1983**, *52*, 2148–2155.
12. Liu, H.; Neal, A. T.; Zhu, Z.; Luo, Z.; Xu, X. F.; Tomanek, D.; Ye, P. D. D. Phosphorene: An Unexplored 2D Semiconductor with a High Hole Mobility. *ACS Nano* **2014**, *8*, 4033–4041.
13. Dai, J.; Zeng, X. C. Bilayer Phosphorene: Effect of Stacking Order on Bandgap and Its Potential Applications in Thin-Film Solar Cells. *J. Phys. Chem. Lett.* **2014**, *5*, 1289–1293.
14. Tran, V.; Soklaski, R.; Liang, Y. F.; Yang, L. Layer-Controlled Band Gap and Anisotropic Excitons in Few-Layer Black Phosphorus. *Phys. Rev. B* **2014**, *89*, 235319.
15. Li, L. K.; Yu, Y. J.; Ye, G. J.; Ge, Q. Q.; Ou, X. D.; Wu, H.; Feng, D. L.; Chen, X. H.; Zhang, Y. B. Black Phosphorus Field-Effect Transistors. *Nat. Nanotechnol.* **2014**, *9*, 372–377.
16. Appalakondaiah, S.; Vaitheeswaran, G.; Lebegue, S.; Christensen, N. E.; Svane, A. Effect of van der Waals Interactions on the Structural and Elastic Properties of Black Phosphorus. *Phys. Rev. B* **2012**, *86*, 035105.
17. Keyes, R. W. The Electrical Properties of Black Phosphorus. *Phys. Rev.* **1953**, *92*, 580–584.
18. Wood, J. D.; Wells, S. A.; Jariwala, D.; Chen, K. S.; Cho, E.; Sangwan, V. K.; Liu, X.; Lauhon, L. J.; Marks, T. J.; Hersam, M. C. Effective Passivation of Exfoliated Black Phosphorus Transistors against Ambient Degradation. *Nano Lett.* **2014**, *14*, 6964–6970.
19. Jariwala, D.; Sangwan, V. K.; Wu, C. C.; Prabhumirashi, P. L.; Geier, M. L.; Marks, T. J.; Lauhon, L. J.; Hersam, M. C. Gate-Tunable Carbon Nanotube–MoS_2 Heterojunction p-n Diode. *Proc. Natl. Acad. Sci. U.S.A.* **2013**, *110*, 18076–18080.
20. Sangwan, V. K.; Arnold, H. N.; Jariwala, D.; Marks, T. J.; Lauhon, L. J.; Hersam, M. C. Low-Frequency Electronic Noise in Single-Layer MoS_2 Transistors. *Nano Lett.* **2013**, *13*, 4351–4355.
21. Buscema, M.; Groenendijk, D. J.; Blanter, S. I.; Steele, G. A.; van der Zant, H. S. J.; Castellanos-Gomez, A. Fast and Broadband Photoresponse of Few-Layer Black Phosphorus Field-Effect Transistors. *Nano Lett.* **2014**, *14*, 3347–3352.
22. Engel, M.; Steiner, M.; Avouris, P. Black Phosphorus Photodetector for Multispectral, High-Resolution Imaging. *Nano Lett.* **2014**, *14*, 6414–6417.
23. Koenig, S. P.; Doganov, R. A.; Schmidt, H.; Neto, A. H. C.; Ozyilmaz, B. Electric Field Effect in Ultrathin Black Phosphorus. *Appl. Phys. Lett.* **2014**, *104*, 103106.
24. Liu, X.; Wood, J. D.; Chen, K. S.; Cho, E.; Hersam, M. C. *In Situ* Thermal Decomposition of Exfoliated Two-Dimensional Black Phosphorus. *J. Phys. Chem. Lett.* **2015**, *6*, 773–778.
25. Chang, Y. H.; Zhang, W.; Zhu, Y.; Han, Y.; Pu, J.; Chang, J. K.; Hsu, W. T.; Huang, J. K.; Hsu, C. L.; Chiu, M. H.; et al. Monolayer $MoSe_2$ Grown by Chemical Vapor Deposition for Fast Photodetection. *ACS Nano* **2014**, *8*, 8582–8590.
26. Docherty, C. J.; Parkinson, P.; Joyce, H. J.; Chiu, M. H.; Chen, C. H.; Lee, M. Y.; Li, L. J.; Herz, L. M.; Johnston, M. B. Ultrafast Transient Terahertz Conductivity of Monolayer MoS_2 and WSe_2 Grown by Chemical Vapor Deposition. *ACS Nano* **2014**, *8*, 11147–11153.
27. Liu, N.; Tian, H.; Schwartz, G.; Tok, J. B.; Ren, T. L.; Bao, Z. Large-Area, Transparent, and Flexible Infrared Photodetector Fabricated Using p-n Junctions Formed by n-Doping Chemical Vapor Deposition Grown Graphene. *Nano Lett.* **2014**, *14*, 3702–3708.
28. Su, G.; Hadjiev, V. G.; Loya, P. E.; Zhang, J.; Lei, S.; Maharjan, S.; Dong, P.; Ajayan, P. M.; Lou, J.; Peng, H. Chemical Vapor Deposition of Thin Crystals of Layered Semiconductor SnS_2 for Fast Photodetection Application. *Nano Lett.* **2015**, *15*, 506–513.
29. Eda, G.; Yamaguchi, H.; Voiry, D.; Fujita, T.; Chen, M.; Chhowalla, M. Photoluminescence from Chemically Exfoliated MoS_2. *Nano Lett.* **2011**, *11*, 5111–5116.
30. Sun, X. M.; Luo, D. C.; Liu, J. F.; Evans, D. G. Monodisperse Chemically Modified Graphene Obtained by Density Gradient Ultracentrifugal Rate Separation. *ACS Nano* **2010**, *4*, 3381–3389.
31. Hernandez, Y.; Nicolosi, V.; Lotya, M.; Blighe, F. M.; Sun, Z.; De, S.; McGovern, I. T.; Holland, B.; Byrne, M.; Gun'Ko, Y. K.; et al. High-Yield Production of Graphene by Liquid-Phase Exfoliation of Graphite. *Nat. Nanotechnol.* **2008**, *3*, 563–568.
32. Coleman, J. N.; Lotya, M.; O'Neill, A.; Bergin, S. D.; King, P. J.; Khan, U.; Young, K.; Gaucher, A.; De, S.; Smith, R. J.; et al. Two-Dimensional Nanosheets Produced by Liquid Exfoliation of Layered Materials. *Science* **2011**, *331*, 568–571.

33. Paton, K. R.; Varrla, E.; Backes, C.; Smith, R. J.; Khan, U.; O'Neill, A.; Boland, C.; Lotya, M.; Istrate, O. M.; King, P.; et al. Scalable Production of Large Quantities of Defect-Free Few-Layer Graphene by Shear Exfoliation in Liquids. *Nat. Mater.* **2014**, *13*, 624–630.
34. Brent, J. R.; Savjani, N.; Lewis, E. A.; Haigh, S. J.; Lewis, D. J.; O'Brien, P. Production of Few-Layer Phosphorene by Liquid Exfoliation of Black Phosphorus. *Chem. Commun.* **2014**, *50*, 13338–13341.
35. Yasaei, P.; Kumar, B.; Foroozan, T.; Wang, C.; Asadi, M.; Tuschel, D.; Indacochea, J. E.; Klie, R. F.; Salehi-Khojin, A. High-Quality Black Phosphorus Atomic Layers by Liquid-Phase Exfoliation. *Adv. Mater.* **2015**, 10.1002/adma.201405150.
36. Eda, G.; Fanchini, G.; Chhowalla, M. Large-Area Ultrathin Films of Reduced Graphene Oxide as a Transparent and Flexible Electronic Material. *Nat. Nanotechnol.* **2008**, *3*, 270–274.
37. Becerril, H. A.; Mao, J.; Liu, Z.; Stoltenberg, R. M.; Bao, Z.; Chen, Y. Evaluation of Solution-Processed Reduced Graphene Oxide Films as Transparent Conductors. *ACS Nano* **2008**, *2*, 463–470.
38. Yau, S. L.; Moffat, T. P.; Bard, A. J.; Zhang, Z. W.; Lerner, M. M. STM of the (010) Surface of Orthorhombic Phosphorus. *Chem. Phys. Lett.* **1992**, *198*, 383–388.
39. Liang, Y. T.; Hersam, M. C. Highly Concentrated Graphene Solutions *via* Polymer Enhanced Solvent Exfoliation and Iterative Solvent Exchange. *J. Am. Chem. Soc.* **2010**, *132*, 17661–17663.
40. Secor, E. B.; Lim, S.; Zhang, H.; Frisbie, C. D.; Francis, L. F.; Hersam, M. C. Gravure Printing of Graphene for Large-Area Flexible Electronics. *Adv. Mater.* **2014**, *26*, 4533.
41. O'Neill, A.; Khan, U.; Nirmalraj, P. N.; Boland, J.; Coleman, J. N. Graphene Dispersion and Exfoliation in Low Boiling Point Solvents. *J. Phys. Chem. C* **2011**, *115*, 5422–5428.
42. Goodman, N. B.; Ley, L.; Bullett, D. W. Valence-Band Structures of Phosphorus Allotropes. *Phys. Rev. B* **1983**, *27*, 7440–7450.
43. Harada, Y.; Murano, K.; Shirotani, I.; Takahashi, T.; Maruyama, Y. Electronic-Structure of Black Phosphorus Studied by X-ray Photoelectron-Spectroscopy. *Solid State Commun.* **1982**, *44*, 877–879.
44. Brunner, J.; Thuler, M.; Veprek, S.; Wild, R. X-ray Photoelectron Study of Amorphous Phosphorus Prepared by Plasma Chemical Transport Comparison with Crystalline Polymorphs. *J. Phys. Chem. Solids* **1979**, *40*, 967–971.
45. Ziletti, A.; Carvalho, A.; Campbell, D. K.; Coker, D. F.; Castro Neto, A. H. Oxygen Defects in Phosphorene. *Phys. Rev. Lett.* **2015**, *114*, 046801.
46. Li, X.; Zhang, G.; Bai, X.; Sun, X.; Wang, X.; Wang, E.; Dai, H. Highly Conducting Graphene Sheets and Langmuir–Blodgett Films. *Nat. Nanotechnol.* **2008**, *3*, 538–542.